Eur. Phys. J. D (2015) 69: 189
DOI: 10.1140/epjd/e2015-60113-9

THE EUROPEAN PHYSICAL JOURNAL D

Regular Article

Double photoionization of helium: a generalized Sturmian approach

Juan M. Randazzo[1,2,a], Darío Mitnik[2,3], Gustavo Gasaneo[2,4], Lorenzo U. Ancarani[5], and Flavio D. Colavecchia[1,2]

[1] División Física Atómica, Molecular y Óptica, Centro Atómico Bariloche, 8400 S. C. de Bariloche, Río Negro, Argentina
[2] Consejo Nacional de Investigaciones Científicas y Técnicas, CONICET, Argentina
[3] Instituto de Astronomía y Física del Espacio, FCEyN Universidad de Buenos Aires, Argentina
[4] Departamento de Física, Universidad Nacional del Sur, 8000 Bahía Blanca, Buenos Aires, Argentina
[5] Théorie, Modélisation, Simulation, SRSMC, UMR CNRS 7565, Université de Lorraine, 57078 Metz, France

Received 19 February 2015 / Received in final form 26 May 2015
Published online 4 August 2015 –

Abstract. In this work we study the double photoionization of helium induced by low intensities laser fields in the regime where only one photon absorption occurs. The method proposed here is based on a Generalized Sturmian Functions (GSF) spectral approach which allows the imposition of outgoing boundary conditions for both ejected electrons. These, in turn, construct an hyperspherical flux characteristic of double continuum wave functions. We compare our calculated cross sections at 20 and 40 eV above threshold with absolute and relative measurements, and with other calculations. Our results definitively demonstrate the applicability of the GSF approach for dealing with break-up Coulomb problems.

1 Introduction

During the last few years we have been working on the development of a spectral approach to solve n-body problems based on the use of Generalized Sturmian Functions (GSF) [1]. With these basis functions we are able to represent a given overall character of the system, whether bound, continuum or a mixture. This is done by imposing proper boundary conditions to the basis functions in the coordinate in which they are defined. Regularity at the origin, for instance Kato cusp conditions, with box boundary conditions or exponential fall off behavior at large distances can be imposed for bound states. Standing-wave, outgoing or incoming flux conditions, including also coordinate-dependent Coulomb phases, can be used for scattering problems. The well-known Coulomb Sturmian Functions (CSF), introduced by Shull and Löwdin [2], correspond to a particular case of GSF. Rotenberg [3,4] used CSF in scattering problems and named them Sturmians due to the similarities with the Sturm-Liouville theory.

The GSF approach has proven to be successful for calculating atomic bound states [5], as well as for stationary (time-independent) scattering states [6–8]. The advantage of a spectral approach over grid methods resides in the reduction of the number of elements needed to represent the wave function. Indeed, the GSF approach is based on the use of functions sets which diagonalize some of the interactions present in the Hamiltonian of the considered problem, and besides, they can be constructed to include appropriate asymptotic conditions. This directly implies a considerable size reduction of the matrix representation of the Hamiltonian and also leads to a substantial reduction in the amount of computational resources needed for the calculations. It is in general not easy to get the desired solution of the Schrödinger equation, especially when the boundary conditions are those related to scattering processes. The GSF approach provides a numerical method which was shown to be successful and efficient in evaluating differential cross sections for S-wave models of $(e, 2e)$ [6,7] and $(e, 3e)$ processes [8]. However, a solution for a full scattering problem using GSF has not yet been presented in the literature. The main aim of this paper is to show that the method is capable to deal with a complete three-body scattering problem, here the double photo-ionization of helium. Our calculated Triple Differential Cross Sections (TDCS) will be compared with experimental $(\gamma, 2e)$ data and also with other theoretical results.

Double photo ionization of helium by one photon absorption has been a subject of interest for a long time. This is due to the fact that this is the simplest process where the emission to the continuum of two electrons can occur. Before and after the photon is absorbed we have a pure three-body problem with no other perturbation. Thus, it is the best test possible when considering a three-body transition from bound to continuum states.

[a] e-mail: randazzo@cab.cnea.gov.ar

Measurements of this and similar systems can be widely found in the literature [9–19]. Most of them have been possible thanks to the use of complete dynamics measurement techniques such as Time of Flight spectrometers [20] or COLTRIMS [21]. From the theoretical point of view there are several approaches, such as hyperspherical partial wave calculations [9], Exterior Complex Scaling (ECS) [22], three-Coulomb-wave approaches (C3) [23,24], Convergent Close Coupling (CCC) calculations [16,25], Time Dependent Close Coupling (TDCC) approaches [26], Hyperspherical R-matrix calculations [27], as well as expansions using complex Sturmian functions in the context of Floquet [28] and time dependent [29] approaches. The comparison of differential cross sections with previously published results will basically demonstrate that the GSF method is as efficient as other techniques, in particular as the ECS. Furthermore, we will show that our method is very efficient in the numerical treatment of the problem; thus it is encouraging for application to other and much more difficult problems such as, e.g., the double ionization of helium by two photon absorption.

This paper is organized as follows. In Section 2 we present the driven equation for the scattering wave function after one photon absorption, and the formulas employed to evaluate the cross sections. In Section 3 we propose a partial wave GSF expansion for the three-body bound and scattering wave functions, and specify the parameters employed to construct the linear system of equations. We also discuss the implementation and convergence properties of the Preconditioned Conjugate Gradient Squared Method we use to find the scattering solution. Then, in Section 4 we present the obtained single and triple differential cross sections and compare them with data from experiments and other theoretical approaches. Finally, in Section 5 a summary is provided.

Atomic units ($\hbar = e = m_e = 1$) are assumed throughout, unless stated otherwise.

2 Theory

In order to describe the dynamics of the double ionization of helium by single photon impact in a time independent scheme, we seek for the scattering wave function $\Psi_{sc}(\mathbf{r}_1, \mathbf{r}_2)$ containing the entangled admixture of all final states. Let the vectors $\mathbf{r}_i$ $(i = 1, 2)$ locate the electrons from the nucleus, which is considered to be at rest at the center of mass; we shall hereafter use the spherical coordinates $(r_i, \theta_i, \varphi_i)$ associated to these two vectors. The scattering wave function can be obtained by solving the non-homogeneous Schrödinger equation in either velocity (V):

$$[H - E]\,\Psi^{+}_{sc,\mathrm{V}}(\mathbf{r}_1, \mathbf{r}_2) = \hat{\varepsilon}.(\bigtriangledown_{\mathbf{r}_1} + \bigtriangledown_{\mathbf{r}_2})\Psi_0(\mathbf{r}_1, \mathbf{r}_2) \quad (1a)$$

or length (L) forms:

$$[H - E]\,\Psi^{+}_{sc,\mathrm{L}}(\mathbf{r}_1, \mathbf{r}_2) = \omega\ \hat{\varepsilon}.(\mathbf{r}_1 + \mathbf{r}_2)\Psi_0(\mathbf{r}_1, \mathbf{r}_2), \quad (1b)$$

where H is the helium Hamiltonian, E is the energy of the system, ω is the photon energy, $\hat{\varepsilon}$ is the polarization vector of the laser; $\Psi_0(\mathbf{r}_1, \mathbf{r}_2)$ is the initial bound state of the atom, with energy E_0, which satisfies:

$$H\Psi_0(\mathbf{r}_1, \mathbf{r}_2) = E_0\Psi_0(\mathbf{r}_1, \mathbf{r}_2). \quad (2)$$

Energy conservation reads $E_0 + \omega = E$.

Equations (1a) and (1b) correspond to the first order term of the Dalgarno-Lewis [30] perturbation series for the Schrödinger equation including the electromagnetic field [31], in the velocity and length gauges respectively. They admit multiple solutions which can be constructed as a linear combination of the particular one and that which satisfies the homogeneous equation. Amongst them, to appropriately describe the physical problem under consideration, we need a wave function possessing an hyperspherical outgoing wave behavior at large distances [32]. This asymptotic behavior is associated to the double ionized electrons, but is always entangled with the single continuum terms. Such a scattering solution, containing all final collision channels at the same time, is unique. The way we solve the non-homogeneous equation (1a) or (1b) will be explained in details in the next section.

To evaluate the physical observables and to extract the physical information from the ionization process we will employ the formulas used in [22]. Suppose the two electrons are emitted into the continuum with momenta $\mathbf{k}_i$ $(i = 1, 2)$, with energies denoted E_1 and E_2 $(E = E_1 + E_2)$. The transition matrix for such process

$$f(\mathbf{k}_1, \mathbf{k}_2) = \left\langle \Phi^{-}(\mathbf{k}_1, \mathbf{r}_1)\Phi^{-}(\mathbf{k}_2, \mathbf{r}_2)|E - T - V(r_1, r_2)\right.$$
$$\left.\times|\Psi^{+}_{sc}(\mathbf{r}_1, \mathbf{r}_2)\right\rangle, \quad (3)$$

is given in terms of the scattering wave function solution of equation (1a) or (1b). The functions $\Phi^{-}(\mathbf{k}_i, \mathbf{r}_i)$ are Coulomb functions normalized to a Dirac δ function in momentum space, T is the system's kinetic energy and $V(r_1, r_2) = -Z/r_1 - Z/r_2$ with $Z = 2$. The operator appearing in the definition of the transition amplitude (3) is the one not solved by the approximated function used as final channel, here a product of uncorrelated Coulomb functions. Employing instead some correlated states would change the matrix element structure, but not its final value if one uses a numerical exact scattering wave function. In this work, and for comparison purposes, we performed the calculations as it was done within the ECS method. Alternative ways of extracting the scattering amplitudes have been explored in the literature. These include for example the use of the outgoing flux associated with the scattering solution, as applied by [27].

The triple differential cross section (TDCS) can be defined in terms of the transition matrix as follows

$$\frac{d^3\sigma}{dE_1 d\Omega_1 d\Omega_2} = \frac{4\pi^2}{\omega c} k_1 k_2 \left|f(\mathbf{k}_1, \mathbf{k}_2)\right|^2, \quad (4)$$

where $d\Omega_i$ denote the solid angles around direction (θ_i, φ_i) for each electron. Integrating over all possible directions one obtains the single differential cross section (SDCS)

$$\frac{d\sigma}{dE_1} = \int \frac{d^3\sigma}{dE_1 d\Omega_1 d\Omega_2} d\Omega_1 d\Omega_2. \quad (5)$$

3 Expansion of the three-body wave functions in GSF

In the present study, we use basis sets composed of two–body radial functions $S_n(r)$, solutions of the Sturmian equation:

$$\left[-\frac{1}{2}\frac{d^2}{dr^2}+\mathcal{U}(r)-E_s\right]S_n(r)=-\beta_n\mathcal{V}(r)S_n(r) \quad (6)$$

where β_n are the eingenvalues. Here E_s is an externally fixed parameter, $\mathcal{U}(r)$ and $\mathcal{V}(r)$ are potentials which can be appropriately chosen to optimize convergence [5]. Equation (6) is solved numerically using a finite-difference scheme and specially adapted diagonalization procedures to avoid numerical instabilities, in particular when complex eigenvalues arise from flux boundary conditions [33]. Such GSF provide a basis and satisfy the potential weighted orthogonality relation

$$\int_0^\infty S_{n'}(r)\mathcal{V}(r)S_n(r)dr\propto\delta_{n,n'}. \quad (7)$$

Three-body solutions to equations (1) and (2) are both obtained through a Sturmian expansion of the form:

$$\Psi(\mathbf{r}_1,\mathbf{r}_2)=\sum_{l_1,l_2}\mathcal{A}_S R^{L,M}_{l_1,l_2}(r_1,r_2)\mathcal{Y}^{L,M}_{l_1,l_2}(\hat{\mathbf{r}}_1,\hat{\mathbf{r}}_2), \quad (8)$$

where

$$R^{L,M}_{l_1,l_2}(r_1,r_2)=\sum_{n_1,n_2}a^{L,M}_\nu\frac{S_{n_1}(r_1)}{r_1}\frac{S_{n_2}(r_2)}{r_2}, \quad (9)$$

with $\nu=\{n_1,n_2,l_1,l_2\}$. Here $a^{L,M}_\nu$ are the expansion coefficients, $\mathcal{Y}^{L,M}_{l_1,l_2}(\hat{\mathbf{r}}_1,\hat{\mathbf{r}}_2)$ are the bispherical harmonics [34] and $\mathcal{A}_S$ is the symmetry operator

$$\mathcal{A}_S\Psi(\mathbf{r}_1,\mathbf{r}_2)=\frac{1}{\sqrt{2}}\left[\Psi(\mathbf{r}_1,\mathbf{r}_2)+(-1)^S\Psi(\mathbf{r}_2,\mathbf{r}_1)\right], \quad (10)$$

for the singlet ($S=0$) or triplet ($S=1$) cases.

Two different radial basis sets, with different asymptotic behaviors, were used: one to describe $\Psi_0(\mathbf{r}_1,\mathbf{r}_2)$ and another one for $\Psi^+_{sc}(\mathbf{r}_1,\mathbf{r}_2)$. In both cases we set as auxiliary potential $\mathcal{U}(r)=-2/r$. For convenience, we have chosen here to not include the centrifugal barriers (see Eq. (6)), in contrast with the choice of previous publications [5,35]. As a consequence, the centrifugal terms are not removed from the coupled equations, obtained upon replacement of expressions (8) into equation (1) and (2). After a projection by the left with the entire basis elements identified by ν' (the Galerkin method [36]), one obtains the Hamiltonian matrix elements:

$$\begin{aligned}[\mathbf{H}]_{\nu,\nu'}=&\Big(\frac{1}{2}l_1(l_1+1)[\mathbf{r_1}^{-2}]_{n_1,n_1'}[\mathbf{O}]_{n_2,n_2'} \quad (11)\\ &+\frac{1}{2}l_2(l_2+1)[\mathbf{r_2}^{-2}]_{n_2,n_2'}[\mathbf{O}]_{n_1,n_1'}\\ &+\beta_{n_1'}[\mathbf{u_1}]_{n_1,n_1'}[\mathbf{O}]_{n_2,n_2'}+\beta_{n_2'}[\mathbf{u_2}]_{n_2,n_2'}[\mathbf{O}]_{n_1,n_1'}\\ &+2E_{s,1}[\mathbf{O}]_{n_1,n_1'}[\mathbf{O}]_{n_2,n_2'}\Big)\delta_{l_1,l_1'}\delta_{l_2,l_2'}+[\mathbf{r}_{12}^{-1}]_{\nu,\nu'}\\ &+(1\leftrightarrow 2),\end{aligned}$$

where the symbol $(1\leftrightarrow 2)$ means the interchange contribution, and the one dimensional integrals are defined as

$$[\mathbf{O}]_{n,n'}=\int_0^\infty S_n(r)S_{n'}(r)dr \quad (12a)$$

$$[\mathbf{r}^p]_{n,n'}=\int_0^\infty S_n(r)r^pS_{n'}(r)dr \quad (12b)$$

$$[\mathbf{u}]_{n,n'}=\int_0^\infty S_n(r)\mathcal{U}(r)S_{n'}(r)dr. \quad (12c)$$

Here, it is worth underlining two points which are characteristic of the Sturmian approach [1]: the overlap matrices $[\mathbf{O}]_{n,n'}$ are always well defined and no conjugation are present (this is also true for the orthogonality property (7)).

For the repulsion matrix element $[\mathbf{r}_{12}^{-1}]_{\nu,\nu'}$ a partial wave decomposition is used [37]:

$$[\mathbf{r}_{12}^{-1}]_{\nu,\nu'}=\sum_{l=0}\frac{4\pi}{2l+1}\left[\frac{r^l_<}{r^{l+1}_>}\right]_{\nu,\nu'}A^{L,l_1',l_2'}_{M,l_1,l_2}, \quad (13)$$

with the matrix elements $A^{L,l_1',l_2'}_{M,l_1,l_2}$ written in terms of Clebsch-Gordan coefficients. Compared to the rest of the matrix elements, the angular integrals $A^{L,l_1',l_2'}_{M,l_1,l_2}$ are not necessary null when $(l_1,l_2)\neq(l_1',l_2')$, and are responsible for the appearance of non-diagonal blocks in $\mathbf{H}$. The matrix elements $\left[\frac{r^l_<}{r^{l+1}_>}\right]_{\nu,\nu'}$ are two dimensional integrals which must be evaluated numerically as the Sturmian basis is numerical. Fortunately, they can be partially uncoupled and finally are equivalent to two one dimensional integrals of rapid evaluation [29]. When compared to the rest of the Hamiltonian, the numerical evaluation of such matrix elements is still the most demanding part, since we have to evaluate one of these integrals for each set $\{l,n_1,n_2,n_1',n_2'\}$. If the centrifugal barriers were included in the radial equation (6), there would be one radial set per partial wave included, and the number of matrix elements to be evaluated would be multiplied by the square of the number of the employed partial wave terms.

For $\Psi_0(\mathbf{r}_1,\mathbf{r}_2)$ ($L=M=S=0$), the radial basis is obtained by setting in equation (6) the negative value $E_s=-2.5$ a.u., yielding a complete set of Sturmian functions with a fall off behavior. The generating potential $\mathcal{V}(r)$ can be chosen in several ways, for instance the sophisticated one given in [5], a choice which provides the correct cusp to the basis and asymptotic conditions associated to the charge of $\mathcal{U}(r)$ (we would then have GSF). Alternatively, by setting $\mathcal{V}(r)=-1/r$, we could use a set of s-wave Coulomb Sturmian functions (CSF). We tried with both options and did not find differences in the calculated cross sections. The results to be presented in Section 4 were evaluated with a properly symmetrized s-wave CSF radial basis of 6 elements for each radial coordinate, with $L=M=0$, $l_1=l_2=0,1,2,3,4$ in equation (8), making a total of 105 orbitals. We obtained energies below $-2.903\,232$ a.u.: this value should be compared to the exact energy $-2.903\,724$ a.u. [34] and, for example, the one

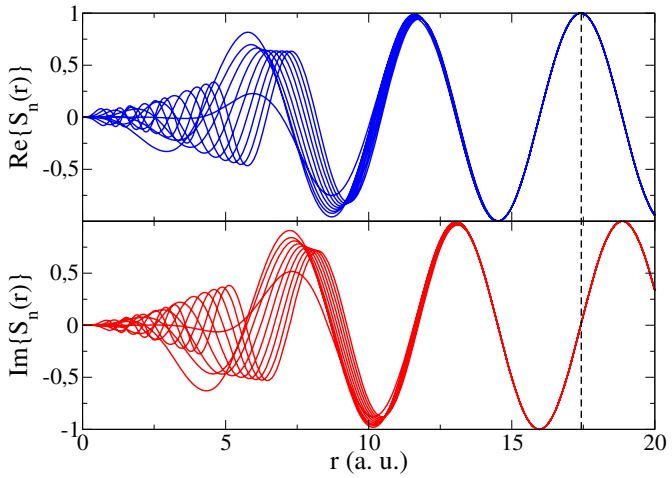

Fig. 1. Typical Generalized Sturmian Functions, here for $n = 1, \ldots, 10$, with outgoing flux conditions imposed at $r = 17.5$ a.u. Top: real part; bottom: imaginary part. At large distances the real and imaginary parts are shifted by $\pi/2$ as clearly seen through the vertical dashed line.

(−2.903 198 a.u.) appearing in the ECS study [22]. The numerical precision with which the bound state is represented is by far enough for the present purposes.

For the scattering wave function $\Psi^+_{sc}(\mathbf{r}_1, \mathbf{r}_2)$, only $L = 1$ and $M = S = 0$ are required. We employed expansion (8) with outgoing flux condition Sturmian basis sets. As in reference [6], we used a basis energy E_s that equals the double continuum energy E of the physical system. Figure 1 shows ten outgoing flux Sturmians, normalized to have the same value at $r = 17.5$ a.u. where boundary conditions are imposed. By construction, from $r = 17.5$ a.u. onwards the basis functions have all the same behavior, and the real and imaginary parts have a phase difference of $\pi/2$ (as the vertical dashed line helps to visualize). We typically employed a square well as a generating potential $\mathcal{V}(r)$, and found it is a good choice for the length gauge calculation. However, in the velocity gauge, due to the behavior of the right hand side of equation (1a) near the $r_1 = r_2 = 0$ region, the convergence rate with such a basis is not as good as for the length gauge. Improvement is obtained by adding a Yukawa potential to $\mathcal{V}(r)$ in order to concentrate the oscillations in that domain. This choice yields accurate results in both gauges. In equation (8) we use $L = 1$, $M = 0$ (as imposed by the right hand side of the non-homogeneous Eq. (1)), $l_1 = l$ and $l_2 = l + 1$ with $l = 0, 1, 2, 3$. Adding more partial wave terms does not change further the values of the TDCS, precisely as observed in reference [22]. The radial domain was chosen to be 35 a.u. (30 a.u.) for $E = 20$ eV (40 eV), for which 35 (37) radial orbitals per coordinate were employed, making a total of 4900 (5476) basis elements. This number can be compared with 11236 as given in page 6 of reference [22]. Since the size of the hamiltonian matrix in a given representation is the square of the basis size, it means that with a GSF expansion one saves about 75 percent in memory storage of the hamiltonian matrix. The reason behind it is that using GSF provides a spectral approach in which the

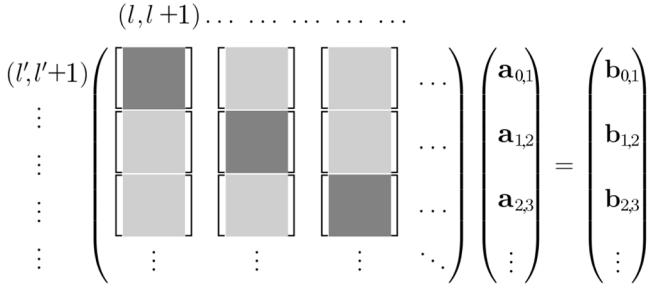

Fig. 2. Block structure of the linear set of equations whose solution gives the expansion coefficients of $\Psi^+_{sc}(\mathbf{r}_1, \mathbf{r}_2)$, where $a_{l,l+1}$ denote $a^{1,0}_\nu$ for a set of n_1, n_2 values.

basis functions are solutions of a physical two-body equation absorbing the kinetic energy, the total energy and part of the potentials of the three-body problem under consideration.

After application of the Galerkin method two separate linear problems arise. For equation (2), one obtains a generalized eigenvalue problem, whose lower energy eigenstate is the ground state of the helium atom [5]. This system is easily solved with routines of the linear algebra package *LAPACK* [38]. Once normalized, the bound state $\Psi_0(\mathbf{r}_1, \mathbf{r}_2)$ is inserted into the driven term of equation (1) to construct another linear system of equations of the form $\mathbf{H}.\mathbf{a} = \mathbf{b}$; $\mathbf{a}$ is the vector of coefficients $a^{L,M}_\nu$ related to $\Psi^+_{sc}(\mathbf{r}_1, \mathbf{r}_2)$, while the vector $\mathbf{b}$ contains the projection of the driven term on the basis functions. Since only pairs $(l, l + 1)$ are allowed, the system has the block structure shown in Figure 2. This new system is well determined, and its solution can also be found with *LAPACK*, or with its distributed memory version *ScaLAPACK* [39]. However we prefer to use iterative methods because they give faster convergence rates; moreover, the matrix structure is such that it can be easily implemented in a single processor by steps if only one sub-block of the matrix is stored in RAM memory at each time. We are testing this routine for the first time here and we plan to use it in the future for larger systems of equations associated to other scattering problems.

We have tested several methods, finding the Preconditioned Conjugate Gradient Squared Method (PCGSM) to be the most stable if an adequate precondition is used. As is suggested in reference [40], a good choice is the solution to the system obtained by replacing all the matrix elements by zeros except the ones belonging to the diagonal blocks, where the blocks are defined by the matrix elements whose angular quantum numbers $\{l', l\}$ are equal. We found for the structure of our matrix blocks (which is intrinsically related to the basis set) that after choosing a random vector $\mathbf{a}^{(0)}$ as a proposal for the solution, the error, defined as the modulus of the vector $(\mathbf{H}.\mathbf{a}^{(m)}) - \mathbf{b}$, decreases by almost one order of magnitude by step (see Fig. 3). We stop the iteration when the error is lower than 10^{-10}.

Typical scattering solutions can be seen in Figure 4 where we have plotted the real and imaginary parts of the

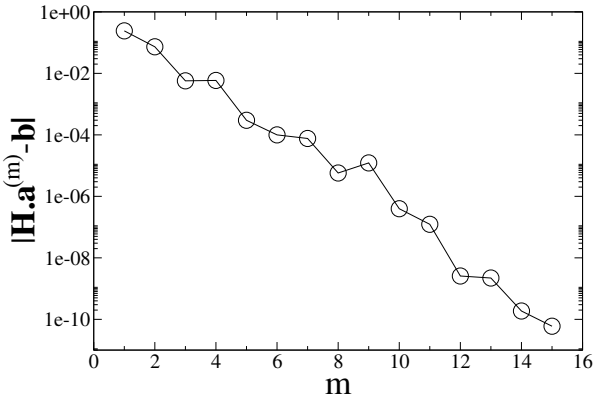

Fig. 3. Convergence of the PCGSM as a function of the iteration step m.

two dimensional radial function $R^{1,0}_{1,2}(r_1, r_2)$ (see Eq. (9)); in order to observe the asymmetry, only the direct contribution is illustrated, i.e., without applying the antisymmetrization operator $\mathcal{A}_S$. Other pairs (l_1, l_2) have been analyzed, and the results coincide – in both shape and magnitude – with those presented in Figure 3 of reference [22]. Note that the partial wave function shown in Figure 4 presents the correct hyperspherical outgoing wave behavior which is built, within our method, from a mixture of products of single-electron outgoing Coulomb waves, each with a given physical momentum.

Once the whole wave scattering function $\Psi^+_{sc}(\mathbf{r}_1, \mathbf{r}_2)$ is constructed through expansion (8), triple and single differential cross sections are evaluated with expressions (3) to (5) and standard integration techniques. A more detailed analysis of the formulas and the expression for each partial wave can be found in reference [22], where it is also explained how the volume integrals can be transformed into surface integrals at a fixed value of the hyperadius.

Before presenting the results, we would like to underline that our GSF approach is very different from those employed in references [29] and [28] where, respectively, time dependent calculation and Floquet theory were implemented through the J-matrix method and Coulomb Sturmian Functions. The J-Matrix approach makes use of energy eigenfunctions, obtained by diagonalizing the three-body Hamiltonian, to represent the internal part of the three-body scattering wave function. For the external part it uses a product of CSF and standing wave Coulomb wave functions. This makes the procedure completely different from the one we are implementing with our GSF. Indeed, we do not need to separate the solution in regions; besides, we generate the basis set so that it incorporates the correct asymptotic behavior and possesses its maximum density in the region where the driven term is located. The cited investigations presented methodologies which explicitly avoid the imposition of boundary conditions in the time dependent case. The evolution of an L^2 initial state (which is not an energy eigenstate) is evaluated at each time step; in the asymptotic region the observables are evaluated from the wave function by means of projection operators. In the Floquet case, the wave

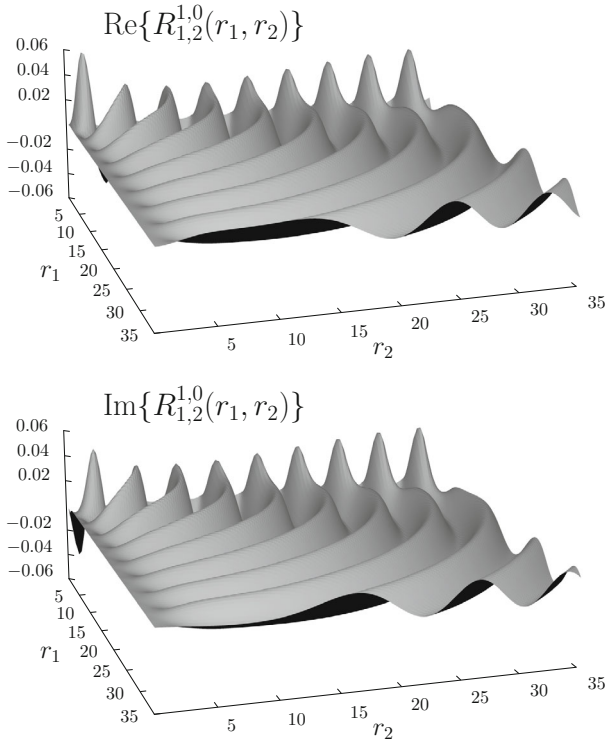

Fig. 4. Real and imaginary parts of the direct contribution of $R^{1,0}_{1,2}(r_1, r_2)$ associated to the second $(l_1 = 1, l_2 = 2)$ partial wave term of Ψ^+_{sc} for $E = 20$ eV.

function is expanded in CSF with complex parameters. We have tested this proposal for electron hydrogen collisions and did not find the smooth hyperspherical outgoing wave behavior as those shown in Figure 4. Instead, we observed noisy surfaces which can be related to an interference between Ψ^+_{sc} with the solution of the homogeneous equation associated to equation (1). Other basis and methods were sought after, and results were summarized in reference [6]. With GSF no additional manipulation (i.e., complex rotation) is applied to the differential equation in order to obtain the desired solution. In summary, the GSF approach used here is completely different from those previously proposed.

4 Cross sections

We have evaluated double photoionization of helium TDCS for $E = 20$ and $E = 40$ eV above threshold. These cross sections are presented below as functions of the polar angle θ_2 of one ejected electron for a fixed θ_1 for the other electron, and this for equal or unequal energy sharing (E_1, E_2).

Accurate and converged calculations should yield the same cross sections (but not the scattering wave function) in both gauges. Our calculated cross sections have this property for all energies and geometries considered in this contribution. An example of TDCS gauge invariance obtained with our numerical method is shown in Figure 5 for $E = 20$ eV.

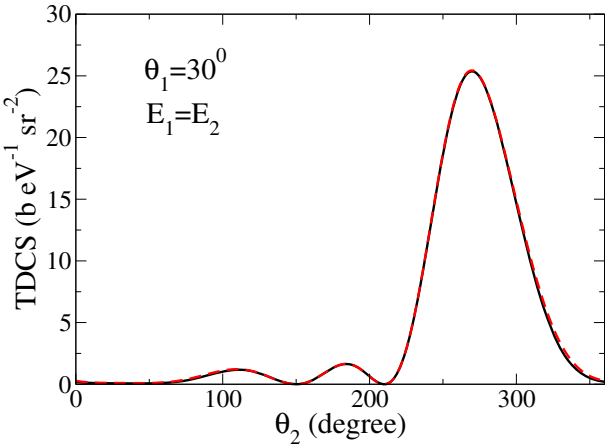

Fig. 5. TDCS calculated in the velocity (solid) and length (dashed) gauges for 20 eV total energy, $E_1 = E_2 = 10$ eV and $\theta_1 = 30°$.

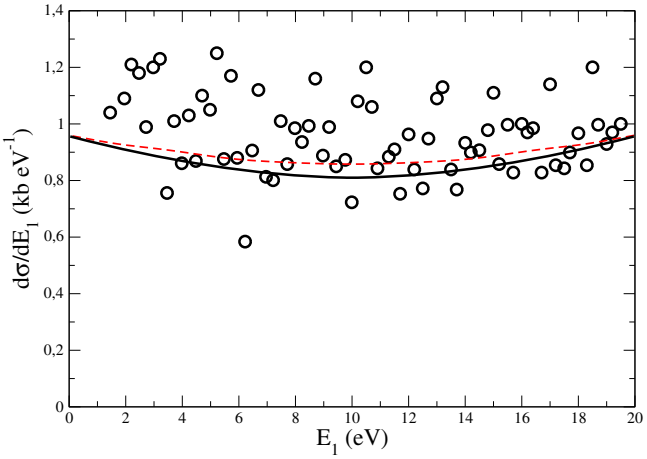

Fig. 6. SDCS for $E = 20$ eV. Circles: experiment by Wehlitz et al. [19]. Red dashed line: ECS calculation [22]. Black solid line: present GSF results.

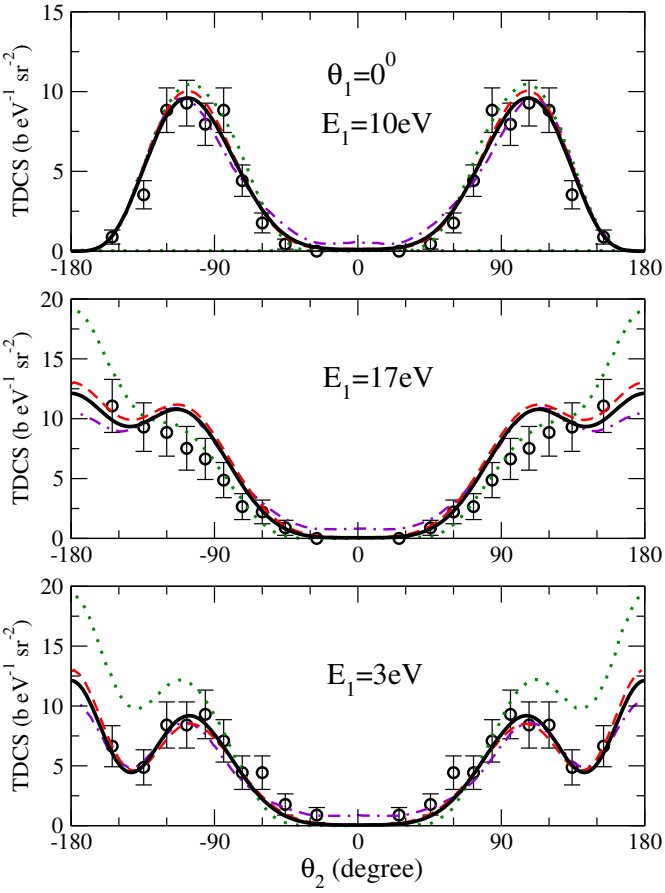

Fig. 7. TDCS for 20 eV energy above threshold for one of the electrons emitted along the polarization axis ($\theta_1 = 0°$) as a function of the polar angle (θ_2) of the secondary electron, for various energy sharing values. Circles: absolute experimental values by Brauning et al. [14]. Red dashed line: ECS calculation [22]. Green dotted line: HRM-SOW calculation [27]. Magenta dot-dashed line: TDCC calculation [26]. Black solid line: present GSF results.

4.1 A 20 eV above threshold

Before describing in detail our TDCS results we show first, in Figure 6, our SDCS result for $E = 20$ eV and compare them with the experimental data of Wehlitz et al. [19] and with the ECS calculations by McCurdy et al.. We see that both theoretical sets lie within the region of experimental dispersion, and a good agreement is found between both methods with a slight discrepancy in the equal energy regime.

Let us now look at the angular distributions of the TDCS. We start by considering the emission of the first electron along the polarization direction ($\theta_1 = 0°$) with energies equal to 10, 17 and 3 eV, as a function of the polar angle θ_2 of the secondary electron. In Figure 7 we compare our TDCS with absolute measurements of Brauning et al. [14]. Comparison is made also with other theoretical results: ECS of McCurdy et al. [22], time dependent close coupling (TDCC) by Colgan et al. [26] and the hyperspherical R-Matrix method with semiclassical outgoing waves (HRM-SOW) by Selles et al. [27]. Our results are in overall good agreement with both experimental data and with other theoretical cross sections. The agreement is particularly noticeable with the ECS and TDCC results, our TDCS lying in-between the two for all energy sharing (except close to $\theta_2 \simeq 100°$ for $E_1 = 3$ eV, where the GSF results are slightly higher than the other two). The HRM-SOW results show some more pronounced differences, in particular close to the Wannier geometry.

The same good agreement can be observed in Figure 8, where we compare TDCS at equal energy sharing for several emission directions of the first electron: $\theta_1 = 0°$, 30°, 60° and 90°. We compare with absolute measurements of Brauning et al. [14] and ECS calculation results of McCurdy et al. [22]. Excellent agreement is found between the two theoretical sets. Agreement is also found with experimental data except at the $\theta_1 = 90°$ geometry, with a theoretical overestimation of the TDCS magnitude.

Results for $\theta_1 = 60°$, 90° and unequal energy sharing ($E_1 = 3$ and 17 eV) are presented in Figure 9, where

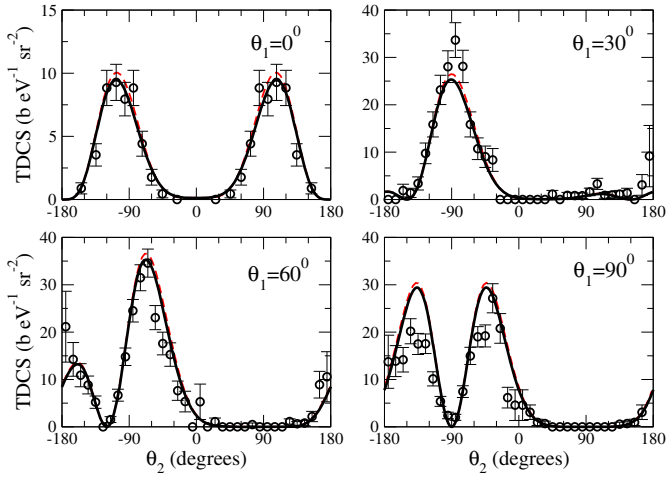

Fig. 8. TDCS for 20 eV and equal energy sharing at various geometries. Circles: absolute experimental values by Brauning et al. [14]. Red dashed line: ECS calculation [22]. Black solid line: present GSF results.

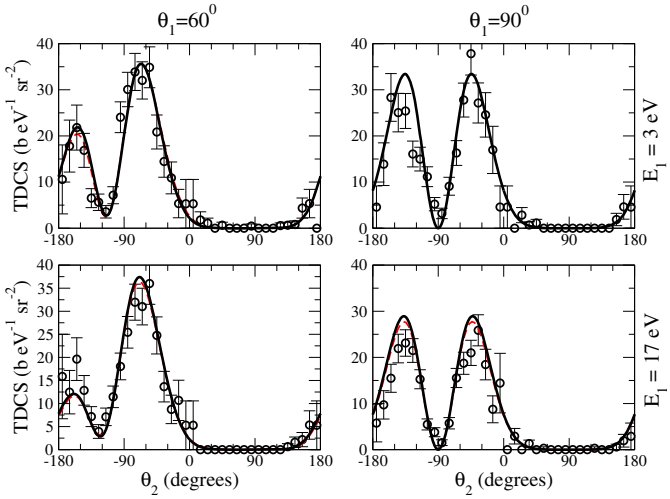

Fig. 9. TDCS for 20 eV at $\theta_1 = 60°, 90°$ and $E_1 = 3$ and 17 eV. Circles: absolute experimental values by Brauning et al. [14]. Red dashed line: ECS calculation [22]. Black solid line: present GSF results.

we compare with Brauning's data and ECS results. Again we observe an excellent agreement between the two theoretical methods (our TDCS are just slightly above ECS results); very good agreement is also found between theories and experiment.

Further detailed TDCS behavior as a function of the energy sharing is shown in Figure 10 for a fixed direction of the first emitted electron ($\theta_1 = 30°$). In this figure, as in Figures 8 and 9, the two theoretical results are virtually indistinguishable.

4.2 A 40 eV above threshold

Let us now consider photoionization at 40 eV above threshold, for which there exist relative measurements from Bolognesi et al. [16] and Cvejanovic et al. [15]. Each experimental data set shown here were scaled to match absolute ECS TDCS results at a given geometry, as done in reference [22], using one scaling parameter for each experimental set.

In Figures 11 and 12 we consider unequal energy sharing given by $E_1 = 5$ eV and its complementary data $E_1 = 35$ eV, for $\theta_1 = 0°$, 30° and 60°. Our GSF results are compared with ECS [22] and CCC [16] calculations. The experimental data [16] were scaled to match the ECS cross section for $\theta_1 = 60°$ and $\theta_2 = 30°$. Our GSF cross sections are in perfect agreement with ECS results, being both theories even more close to each other than in the previous 20 eV above threshold case. Both are in an overall good agreement with the measurements. On the other hand, discrepancies between the CCC and GSF (or ECS) results are more significant. This is true not only in magnitude (see, e.g., the $\theta_1 = 30°$ case in Fig. 11, where differences appear in the peaks ratio), but also in shape (see, e.g., the $\theta_1 = 0°$ case in Fig. 12).

A similar picture is obtained when we consider the relative experiments performed by Cvejanovic et al. [15]. In Figures 13 and 14 we compare experimental TDCS for energy sharing set by $E_1 = 5$ eV at larger values of θ_1 varying from 130° to 180°. These results were scaled to match theoretical ECS cross section at $\theta_1 = 130°$ and $\theta_2 = 250°$. We also include CCC results [41]. Again, a beautiful coincidence is observed between the results of the ECS and GSF methods.

5 Summary

In this work we have presented a numerical solution of the driven Schrödinger equation describing the helium double photo ionization by single photon absorption, in the time independent approach. Both the initial state and the scattering three-body wave function are proposed as a partial wave expansion composed of two-body Generalized Sturmian Functions with appropriate boundary conditions. For the initial bound state we used, for each electron, exponentially decaying behavior corresponding to an electron bound in the central Coulomb potential. For the scattering wave function we used an outgoing-wave behavior associated to a particle escaping from the charged nucleus. The angularly coupled expansion builds up the outgoing hyperspherical wave behavior of the three-body wave function describing the scattering.

From the numerical GSF solution of the scattering wave function we have extracted triple and single differential cross sections for 20 and 40 eV total energy. For both cases, and for all considered geometries, we found TDCS gauge invariance. All our results were compared with ECS calculations by McCurdy et al. [22] and excellent agreement was found; it is worth recalling that we are solving the same driven equation.

Both theoretical sets compare very well, at 20 eV, with the experimental TDCS data of Brauning et al. [14] and with the SDCS measured by Wehlitz et al. [19]. At very unequal energy sharing, the HRM-SOW calculations by

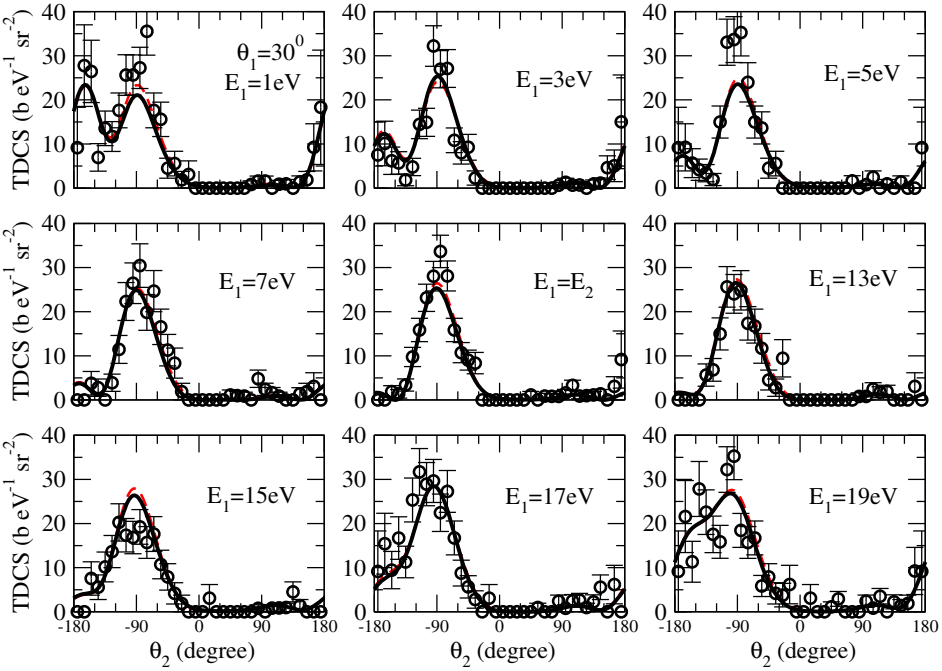

Fig. 10. TDCS for 20 eV at $\theta_1 = 30°$ for several energy sharing regimes. Circles: absolute experimental values by Brauning et al. [14]. Red dashed line: ECS calculation [22]. Black solid line: present GSF results.

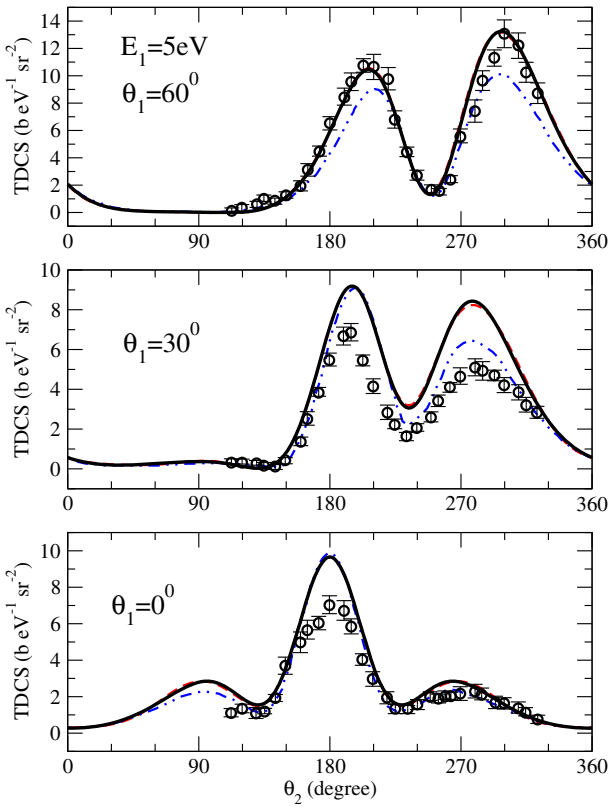

Fig. 11. TDCS for 40 eV photon energy above threshold for energy sharing corresponding to $E_1 = 5$ eV for $\theta_1 = 0°$, 30° and 60°. Circles: experimental values of Bolognesi et al. [16]. Blue dashed-double dotted line: CCC calculation [16]. Red dashed line: ECS calculation [22]. Black solid line: present GSF results.

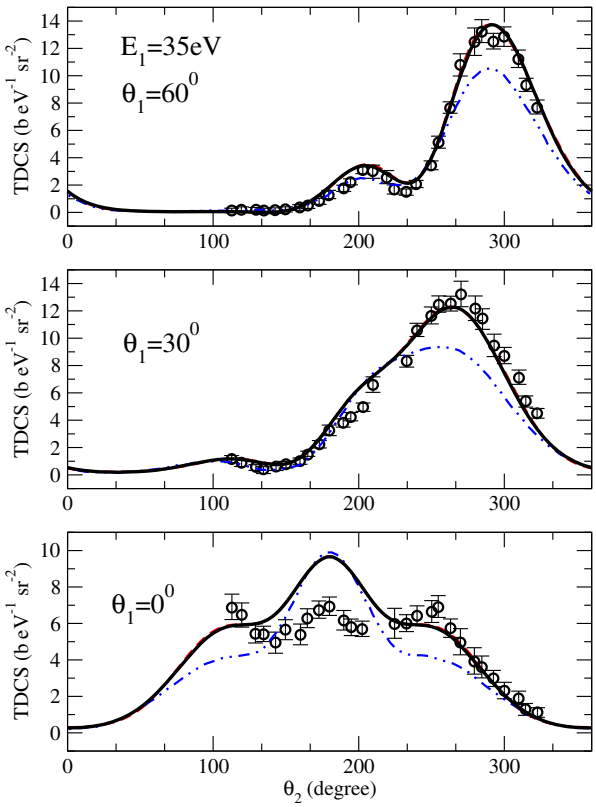

Fig. 12. TDCS for 40 eV photon energy above threshold for energy sharing corresponding to $E_1 = 35$ eV for $\theta_1 = 0°$, 30° and 60°. Circles: experimental values of Bolognesi et al. [16]. Blue dashed-double dotted line: CCC calculation [16]. Red-dashed line: ECS calculation [22]. Black solid line: present GSF results.

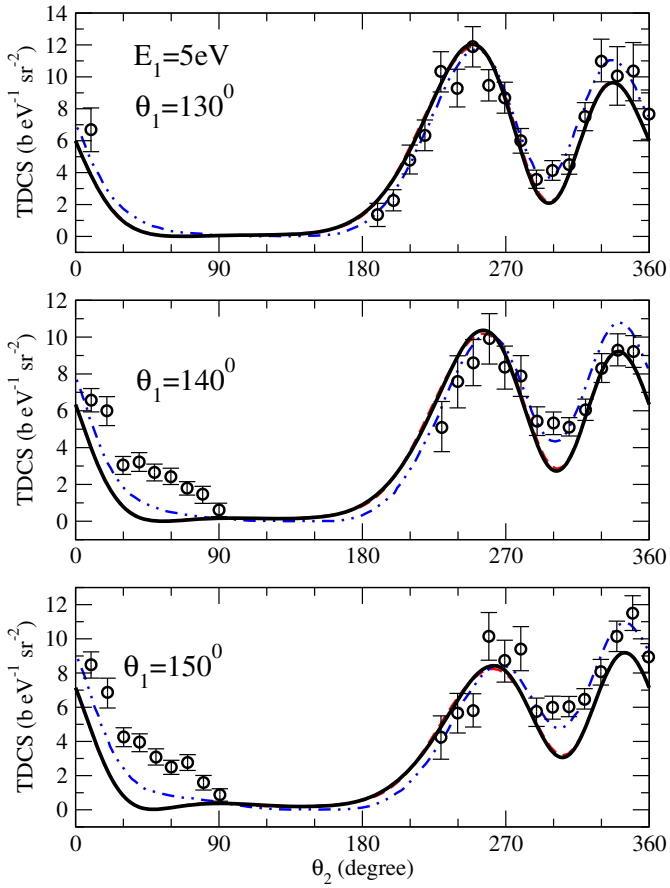

Fig. 13. TDCS for 40 eV photon energy above threshold with $E_1 = 5$ eV and $\theta_1 = 130°$, 140° and 150°. Circles: experiments of Cvejanovic et al. [15]. Blue dashed-double dotted line: CCC calculation [41]. Red dashed line: ECS calculation [22]. Black solid line: present GSF results.

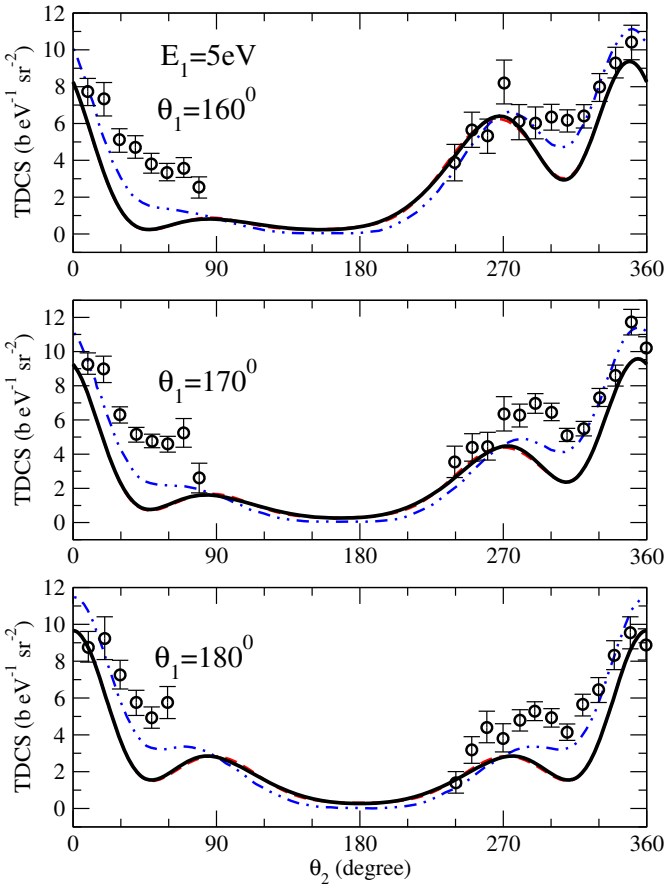

Fig. 14. TDCS for 40 eV photon energy above threshold with $E_1 = 5$ eV and $\theta_1 = 160°$, 170° and 180°. Circles: experiments of Cvejanovic et al. [15]. Blue dashed-double dotted line: CCC calculation [41]. Red dashed line: ECS calculation [22]. Black solid line: present GSF results.

Selles et al. [27] and the TDCC by Colgan et al. [26] show some differences with respect to our results, in particular when the electrons are emitted in opposite directions.

For the 40 eV case, and several geometrical situations, we have compared our TDCS with ECS calculations by McCurdy et al. [22], and with measurements and CCC calculations published by Bolognesi et al. [16] and Cvejanovic et al. [15]. While some discrepancies are noticed with the experiment, on one side, and with the CCC results, on the other side, a beautiful agreement is observed between GSF and ECS methods.

We have verified, in all kinematical and geometrical cases, that adding partial waves beyond $l_1 = 3$ does not affect the TDCS results. Thus, the differences observed between GSF cross sections and experimental data are not due to a lack of convergence.

Finally, we may say that the present study showed that the GSF approach can be successfully used as an efficient numerical tool to construct correctly a three-body scattering solution, and hence to solve three-body break-up problems. Here, we illustrated this through the detailed analysis of $(\gamma, 2e)$ processes on helium.

We would like to thank to Professor C.W. McCurdy for providing the data for comparison. We acknowledge the CNRS (PICS project No. 06304) and CONICET (project No. Dl 158114) for funding. The support by ANPCyT (PICT08/0934) (Argentina) and PIP 607 CONICET (Argentina) is acknowledged. G. Gasaneo also thanks the support by PGI (24/F049) of the Universidad Nacional del Sur. F.D. Colavecchia and J.M. Randazzo thank the support of Universidad Nacional de Cuyo through Grant 06/624.

References

1. G. Gasaneo et al., Adv. Quantum Chem. Chap. **67**, 153 (2013)
2. H. Shull, P.O. Löwdin, J. Chem. Phys. **30**, 617 (1959)
3. M. Rotenberg, Ann. Phys. **19**, 262 (1962)
4. M. Rotenberg, Adv. At. Mol. Phys. **6**, 233 (1970)
5. J.M. Randazzo, L.U. Ancarani, G. Gasaneo, A.L. Frapiccini, F.D. Colavecchia, Phys. Rev. A **81**, 042520 (2010)
6. J.M. Randazzo, F. Buezas, A.L. Frapiccini, F.D. Colavecchia, G. Gasaneo, Phys. Rev. A **84**, 052715 (2011)
7. A.L. Frapiccini et al., J. Phys. B **43**, 101001 (2010)

8. G. Gasaneo, D.M. Mitnik, J.M. Randazzo, L.U. Ancarani, F.D. Colavecchia, Phys. Rev. A **87**, 042707 (2013)
9. J.N. Das, K. Chakrabarti, S. Paul, J. Phys. B **36**, 2707 (2003)
10. R. Dörner et al., Phys. Rev. Lett. **76**, 2654 (1996)
11. R. Wehlitz et al., J. Phys. B **30**, L51 (1997)
12. J.A.R. Samson et al., Phys. Rev. A **57**, 1906 (1998)
13. V. Mergel et al., Rev. Lett. **80**, 5301 (1998)
14. H. Bräuning et al., J. Phys. B **31**, 5149 (1998)
15. S. Cvejanovic et al., J. Phys. B **33**, 265 (2000)
16. P. Bolognesi et al., J. Phys. B **34**, 3193 (2001)
17. J.P. Wightman, S. Cvejanovic, T.J. Reddish, J. Phys. B **31**, 1753 (1998)
18. K. Soejima, A. Danjo, K. Okuno, A. Yagishita, Phys. Rev. Lett. **83**, 1546 (1999)
19. R. Wehlitz et al., Phys. Rev. Lett. **67**, 3764 (1991)
20. J. Mazeau, P. Selles, D. Waymel, A. Huetz, Phys. Rev. Lett. **67**, 820 (1991)
21. J. Ullrich et al., J. Phys. B **30**, 2917 (1997)
22. C.W. McCurdy, D.A. Horner, T.N. Rescigno, F. Martín, Phys. Rev. A **69**, 032707 (2004)
23. F. Maulbetsch, J.S. Briggs, J. Phys. B **26**, 1679 (1993)
24. D. Proulx, R. Shakeshaft, Phys. Rev. A **48**, R875 (1993)
25. A.S. Kheifets, I. Bray, J. Phys. B **31**, L447 (1998)
26. J. Colgan, M.S. Pindzola, F. Robicheaux, J. Phys. B **34**, L457 (2001)
27. P. Selles, L. Malegat, A.K. Kazansky, Phys. Rev. A **65**, 032711 (2002)
28. M. Pont, R. Shakeshaft, Phys. Rev. A **51**, 494 (1995)
29. E. Foumouo, G.L. Kamta, G. Edah, B. Piraux, Phys. Rev. A **74**, 063409 (2006)
30. T.K. Nandi et al., J. Phys. A **29**, 1101 (1996)
31. F.L. Yip, *Efficient Representations of Continuum States for Photoionization Processes from Atomic and Molecular Targets*, Ph.D. thesis, University of California, Berkeley, 2008
32. R. Peterkop, *Theory of ionization of atoms by electron impact* (Colorado Associated University Press, Boulder, 1977)
33. D.M. Mitnik et al., Comput. Phys. Commun. **182**, 1145 (2011)
34. G.W.F. Drake, *Springer Handbook of Atomic, Molecular, and Optical Physics* (Springer, New York, 2006)
35. J.M. Randazzo, A.L. Frapiccini, F.D. Colavecchia, G. Gasaneo, Phys. Rev. A **79**, 022507 (2009)
36. G.I. Marchuk, *Methods of numerical mathematics*, 1st edn. (Springer, New York, 1982)
37. B.H. Bransden, C.J. Joachain, *Physics of atoms and molecules* (Addison-Wesley, Harlow, 2003)
38. E. Anderson et al., D. *LAPACK Users' Guide* (Society for Industrial and Applied Mathematics, Philadelphia, 1999)
39. L. Blackford et al., *ScaLAPACK Users Guide* (Society for Industrial and Applied Mathematics, Philadelphia, 1997)
40. M. Baertschy, T.N. Rescigno, W.A. Isaacs, X. Li, C.W. McCurdy, Phys. Rev. A **63**, 022712 (2001)
41. A.S. Kheifets, I. Bray, Phys. Rev. A **65**, 022708 (2002)